ANL-19/25

PTT System Design and Data Analysis for Improved Performance

Pulsed Thermal Tomography Nondestructive Examination of Additively Manufactured Reactor Materials and Components

Nuclear Science and Engineering Division

ANL-19/25

PTT System Design and Data Analysis for Improved Performance

Pulsed Thermal Tomography Nondestructive Examination of Additively Manufactured Reactor Materials and Components

prepared by
Alexander Heifetz[1], Tiffany Liu[1,2], Dmitry Shribak[1,3]

[1]Nuclear Science Engineering Division, Argonne National Laboratory
[2]Department of Physics, University of California, Berkeley, Berkeley, CA
[3]Department of Physics, University of Chicago, Chicago, IL

August 16, 2019

Table of Contents

List of Figures

List of Tables

Abstract

Additive manufacturing (AM, or 3D printing) for commercial nuclear energy applications is an emerging method for cost-efficient manufacturing aimed at replacing aging nuclear reactor parts and reducing costs for new construction. Because of the geometry of metallic structures of interest for nuclear applications, which consist of planar primitives with no symmetry of revolution, limited options are available for non-destructive evaluation (NDE) either during or post manufacturing. Known material flaws in AM include low density regions consisting of non-sintered powder, which have to be detected to ensure the safety of long-term performance nuclear reactor components. As a solution to NDE of AM, we are developing pulsed thermal tomography (PTT) models and depth inversion algorithms for 3D imaging. PTT has many advantages because the method is non-contact and allows for in-service, NDE of AM nuclear reactor parts. By analyzing transients of surface temperature response due to internal thermal resistances, one can obtain 3D reconstructions of material effusivity using a unique inversion algorithm developed at Argonne. This study investigates the limits of PTT capability in detection of defects in metallic plates using COMSOL numerical modeling of heat transfer. Defects are modeled as cylindrical flat bottom holes (FBH), which is a common model of calibrated material flaws in thermal tomography experiments. Materials considered in this study include stainless steel 316 (SS316), stainless steel 304 (SS304), and Inconel 718. Theoretical analyses were conducted to validate inversion of simulated PTT data with COMSOL for a plate. Subsequently, 3D reconstructions were performed on COMSOL simulations for FBH, revealing a decrease in spatial resolution over depth due to thermal diffusion. The results of this study show that the performance of the inversion algorithm for detecting smaller defects depends strongly on the depth of the defect as well as the incident heat flux. The size of detectable defect was estimated by fitting a Gaussian function to surface temperature profile. The criteria for detectability was taken as 20mK noise equivalent temperature difference (NETD), which is currently the sensitivity limit of high-performance infrared cameras. It was determined through computer simulations that the smallest detectable FBH in SS316 has a 50μm diameter and is located 0.5mm below the plate surface.

1. Introduction

1.1. Background

Additive manufacturing (AM or 3D printing) is a versatile manufacturing method which is expected to play an increasing role in nuclear energy sustainability especially as commercial nuclear reactors start to age. The capabilities of AM for nuclear engineering applications continue to advance, with recent studies investigating 3D printing of different structural components using stainless steel and nickel super alloys [Bertali 2015, Cunningham 2017, Freyer 2018, Kempen 2011] – however, there are still challenges for widespread deployment of AM in nuclear reactors, particularly the ability to perform NDE of AM parts. Because of the intrinsic features of the AM process for fabricating metallic parts, such as direct laser sintering, defects can appear as low-density regions consisting of non-sintered powder due to lack of fusion cause by inadequate melt pool overlap [Lewandowski 2016, Sames 2016, Zhao 2017]. The low-density flaw is potentially a seed for crack formation in the structure due to non-uniform expansion of the material in response to thermal and mechanical stresses in nuclear reactors [Wakamatsu 1995].

Currently, there exist limited options for NDE of AM structures either during or post-manufacturing. The objective of present work is to develop capabilities to perform NDE in post-manufacturing. AM structures for nuclear energy applications are typically composed of planar geometrical primitives. Because of the lack of symmetry, digital radiography, such as X-ray computed tomography (CT) is difficult to perform. Ultrasonic tomography may require many hours of scanning the structure with a direct-contact probe. The surface of a 3D printed metallic part typically has a rough finish due to the nature of AM. This creates a challenge in coupling a high-frequency ultrasonic probe. On the other hand, pulsed thermal tomography (PTT) allows for one-sided, non-contact imaging of large sections of the material.

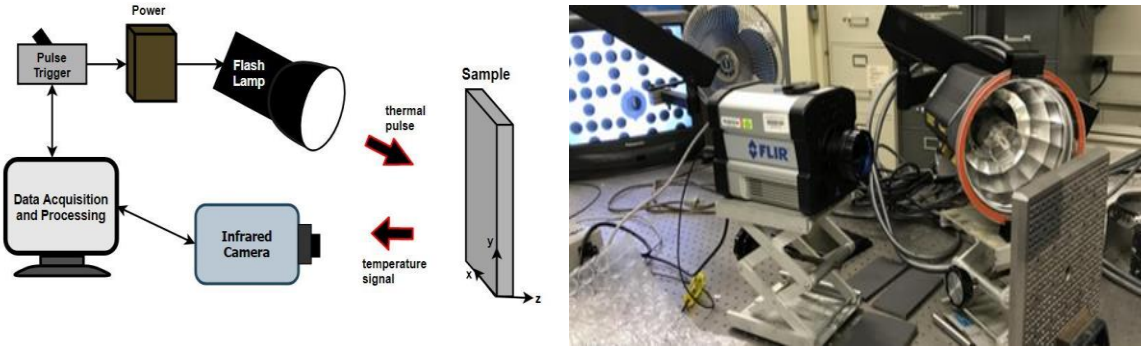

(a) (b)

Figure 1 – Principle of pulsed thermal tomography: (a) Schematic drawing (b) Photograph of actual laboratory system

A schematic depiction of the PTT setup and a photograph of the laboratory system are shown in Figure 1. The method consists of illuminating the material with a white light flash lamp, which rapidly deposits heat on the material surface. A megapixel fast frame infrared (IR) camera records time-resolved images of surface temperature distribution T(x,y,t). As heat propagates from the

surface to interior of the plate, localized “hot spots” appear on the surface of the material. Heat conduction rate decreases around a defect of higher thermal resistance such as air or low-density powder, resulting in the pooling of heat around the defect visible on the surface. These “hot spots” appear earlier for defects located closer to the surface and can vary in appearance depending on the shape of the defect. The reconstruction algorithm obtains depth distribution of thermal effusivity e(x,y,z) from measurements of time-dependent surface temperature T(x,y,t).

1.2. Overview

In this study, we used COMSOL computer simulations with the Heat Transfer module to investigate the performance of the PTT method in detection and 3D reconstruction of flaws in materials used for AM for nuclear energy applications. Computer simulations were performed to model the PTT system depicted in Figure 1. We represented defects as cylindrical flat bottom holes (FBH) with varying sizes and located at various depths. FBH is a common model of calibrated material defects in thermal tomography experiments [Heifetz 2019, Sun 2016]. In computer simulations, surface temperature transient data T(x,y,t) was calculated with COMSOL, and reconstruction of 3D material effusivity e(x,y,z) was performed with an inversion algorithm developed at Argonne and implemented in MATLAB. Transverse size of defects was estimated from surface temperatures by fitting a Gaussian curve and applying detection threshold equal to noise equivalent temperature difference (NETD) of existing state-of-the-art IR cameras. Based on simulation results, we conclude that the inversion algorithm is more suitable for depth detection, while transverse size (radius) of the defect can be efficiently obtained from surface temperature. Effectiveness of 3D reconstruction depended greatly on the depth of the defect as well as incident heat flux, which affects temperature contrast in the image. Further studies using spherical defects were also performed to model more realistic defects observed in AM parts. Materials modeled in COMSOL computer simulations included high strength corrosion-resistant stainless steel (SS) 316 and 304, and Inconel 718 alloys, which are commonly used materials for liquid sodium and light water cooled reactors, respectively [Kultgen 2018]. Temperature-dependent values of density, heat capacity, and thermal conductivity of respective materials were used in computer simulations to account for appreciable changes in material properties over a wide temperature range [Kim 1975].

2. Mathematical Basis of Pulsed Thermal Tomography

2.1. Thermal Tomography Inversion Algorithm

The reconstruction algorithm of pulsed thermal tomography (PTT) obtains thermal effusivity e(z) as a function of depth (z) from time-dependent surface temperature T(t) measurements or that from simulation data. Under ideal thermal tomography conditions, the theoretical model for the algorithm is based on the solution to the 1D heat conduction equation. Heat propagation through the metallic plate is approximately one-dimensional for an instantaneous, uniform pulse of thermal energy.

The algorithm starts with the assumption that the medium can be treated as semi-infinite, with corrections developed during reconstruction. For semi-infinite slabs, heat diffusion can be modeled with 1D equation

$$\frac{\partial T}{\partial t} = \alpha \frac{\partial^2 T}{\partial z^2} \tag{1}$$

where z is the depth coordinate, x and y are coordinates in the transverse plane, and α is thermal diffusivity defined as

$$\alpha = k/\rho c \tag{2}$$

Here, k is thermal conductivity, ρ is density, and c is specific heat. The analytic solution is given as [Sun 2016, Balageas 1986, Parker 1961]

$$T(z,t) = \frac{Q}{\sqrt{\rho c k \pi t}} e^{-\frac{z^2}{4\alpha t}},\ 0 \le z \le \infty \tag{3}$$

where Q is the instantaneously deposited surface thermal energy density (J/m^2), and e is the thermal effusivity, which is a measure of how the material exchanges thermal energy with its surroundings given as

$$e = \sqrt{\rho c k} \tag{4}$$

This allows one to express observed or apparent time-dependent effusivity of the medium as

$$e(t) = \frac{Q}{T(z=0,t)\sqrt{\pi t}} \tag{5}$$

One can calculate the maximum of thermal wavefront velocity $\partial T/\partial z$ by setting

$$\frac{\partial^2 T}{\partial z^2} = 0 \tag{6}$$

which gives characteristic relationship between time and depth

$$z = \sqrt{\pi \alpha t} \tag{7}$$

The next crucial step is to recognize that e(z) and e(t) can be related through a convolution integral, where 1/z is the transfer function [Sun 2016]

$$e(t) = \int_0^z z^{-1} e(\zeta) d\zeta \tag{8}$$

Taking z-derivatives of both sides,

$$e(z) = \frac{d}{dz}\left(ze(t)\right) = \frac{d}{dz}\left(\frac{zQ}{T(t)\sqrt{\pi t}}\right) \tag{9}$$

one can simplify the equation by using Eqn. (7) to obtain

$$e(z) = \frac{d}{dz}\left(\frac{\sqrt{\alpha}Q}{T(t)}\right) \tag{10}$$

To calculate the derivate, one has to relate dz to dt using Eqn. (7)

$$dz = \frac{\sqrt{\pi\alpha}}{2\sqrt{t}}dt = \frac{\sqrt{\pi\alpha}}{2}\frac{\sqrt{\pi\alpha}}{z}dt = \frac{\pi\alpha}{2z}dt \tag{11}$$

Therefore, the z-derivative of a function f can be written as

$$\frac{df}{dz} = \frac{df}{dt}\frac{dt}{dz} = \frac{2z}{\pi\alpha}\frac{df}{dt} \tag{12}$$

such that the final equation is

$$e(z) = z\frac{2Q}{\pi\sqrt{\alpha}}\frac{d}{dt}\left(\frac{1}{T(t)}\right)\Bigg|_{t=z^2/\pi\alpha} \tag{13}$$

so that spatial reconstruction of effusivity is given as a product of depth function z and time derivative of the inverse of surface temperature evaluated at time t corresponding to depth z according to Equation (7).

2.2. Validation of Effusivity Reconstruction from COMSOL Simulated Data

Before analyzing detection of small defects with COMSOL, fidelity of COMSOL simulated data was evaluated by performing of reconstruction for a structure for which there exists a closed form analytical solution. An example chosen in this study is a plate with infinite transverse dimensions and finite thickness L, for which the analytic solution for transient surface temperature as a function of time is given as [Sun 2014, Sun 2016]

$$T(z=0,t)=\frac{Q}{\rho cL}\left[1+2\sum_{n=1}^{\infty}\exp\left(-\frac{n^2\pi^2}{L^2}\alpha t\right)\right] \tag{14}$$

Here T(t) is the change in temperature relative to the value before the thermal impulse Q was applied. Note that the steady-state temperature T=Q/ρcL is a restatement of the familiar expression q=mcΔT for a plate. Generating data for T(t) using Equation (14), one can perform reconstruction procedure using Equation (13). For reference, actual effusivity e(z) given as

$$e(z)=\begin{cases}\sqrt{\rho ck}, & 0\le z\le L\\ 0, & z>L\end{cases} \tag{15}$$

Validations of COMSOL data inversion involved modeling heat diffusion in a 5cmx5cmx0.5cm SS316 plate. Diffusion of heat in a plate with such geometry (transverse dimensions are 10x larger than the thickness) closely resembles the case of an infinite plate of finite thickness. Using the inversion algorithm, thermal effusivity using COMSOL surface temperature data and the analytic solution for temperature decay were compared. For direct comparison with the analytical model, thermophysical properties of SS316 in the COMSOL model were kept constant.

Figure 2 shows reconstructions of e(z) for L=5mm SS316 plate with ρ=7954 kg/m^3, k=13.96 W/m*K, c = 499.07 J/kg. The graphs are plotted for exact effusivity given by Equation 15, effusivity reconstructed from the analytical model of Equation 14, and effusivity reconstructed from COMSOL simulation data. Figure 3 shows exact effusivity e(x,z) plotted as 3D surface and 2D pseudo-color image. Figure 4 shows effusivity reconstructed from the analytical model plotted as 3D surface and 2D pseudo-color image. Figure 5 shows effusivity e(x,z) reconstructed from COMSOL heat transfer simulations, which is plotted as 3D surface and 2D pseudo-color image. Note that reconstruction of effusitvity either from the analytical model or from COMSOL simulations is an approximation which smooths out the sharp edge in the back of the metallic plate. Effusivity reconstruction from COMSOL simulations have a delayed rise at the front surface of the plate, and contain ripples. We attribute that to simulated data artifacts, particularly the

temperature sampling rate. Temperature data for COMSOL simulations in Figures 2 and 5 was sampled at 0.005s intervals. We observed that quality of reconstruction was lower for lower sampling frequency. Sampling at higher rate was challenging because of limited computer workstation memory (64GB). We conclude that, when the known artifacts in the data are taken into account, COMSOL can be used as a data generation platform for analyzing PTT performance.

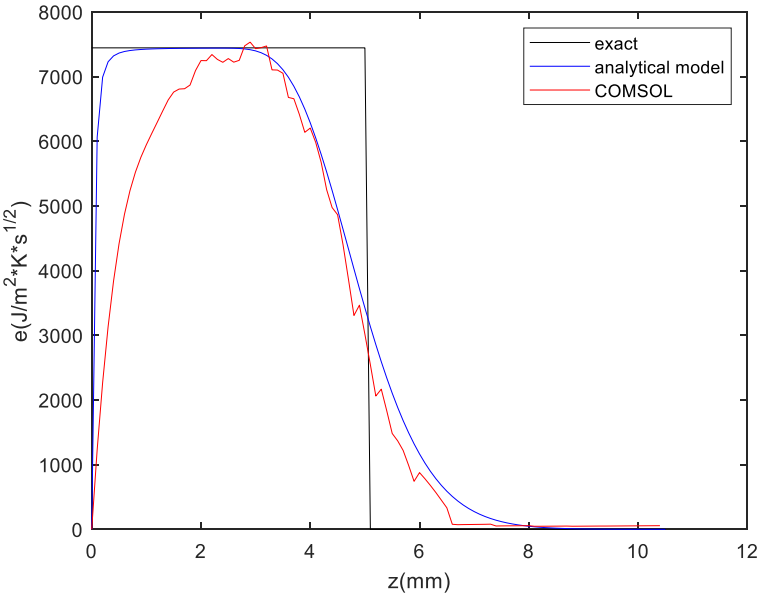

Figure 2 – Effusivity e(z) for L=5mm SS316 plate for exact, reconstruction of from analytical model, and reconstruction from COMSOL simulations

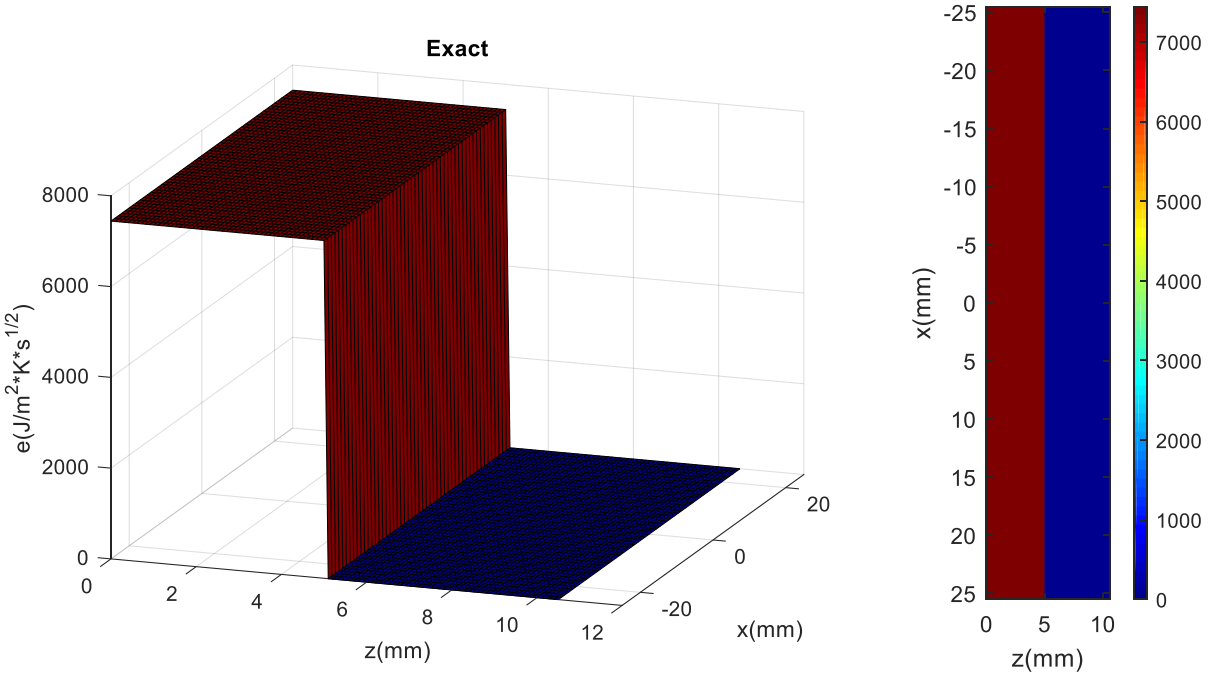

(a) (b)

Figure 3 – Exact effusivity for L=5mm SS316 plate: (a) Surface plot of e(x,z) (b) Pseudo-color image of e(x,z)

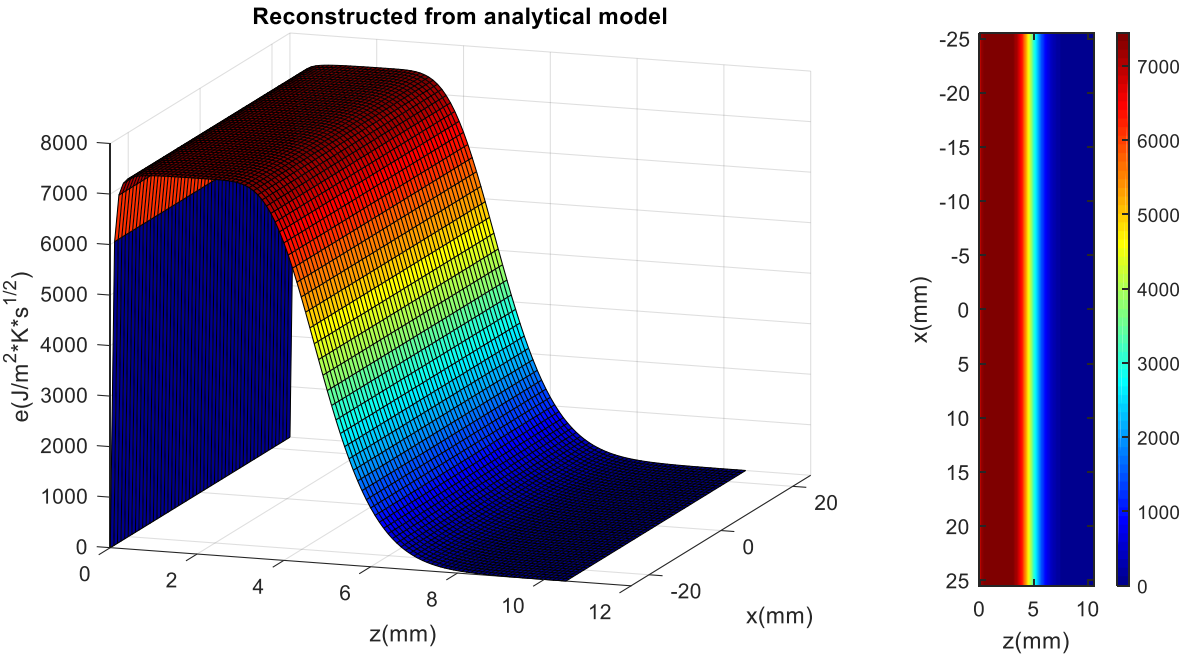

(a) (b)

Figure 4 – Reconstructed effusivity from analytical model for L=5mm SS316: (a) Surface plot of e(x,z) (b) Pseudo-color image of e(x,z)

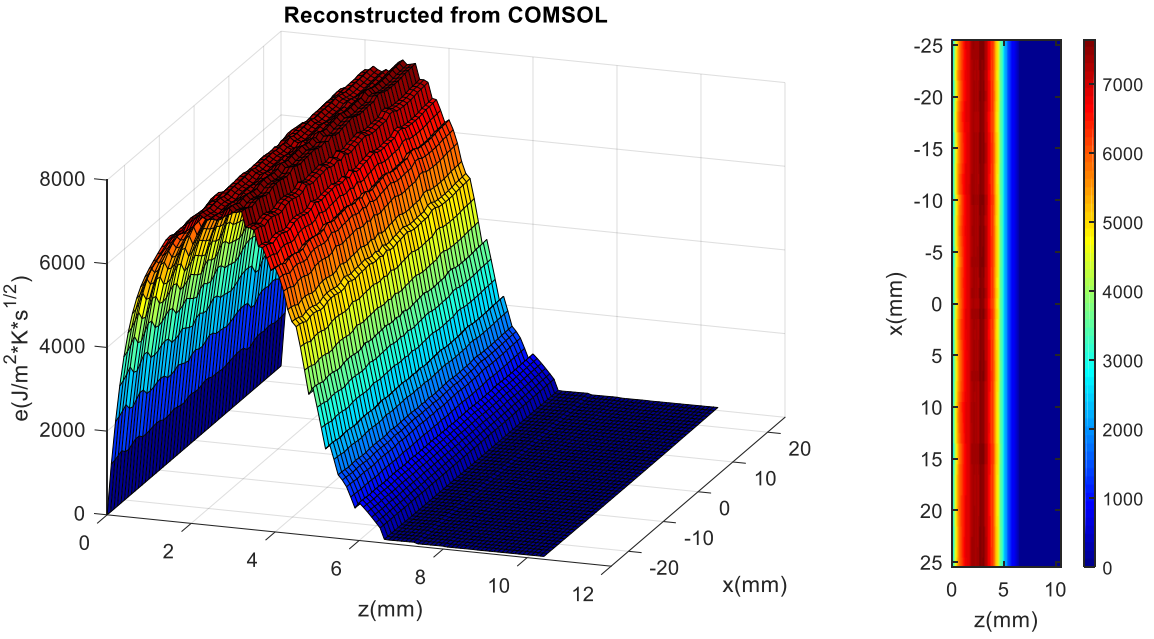

(a) (b)

Figure 5 – Reconstructed effusivity from COMSOL heat transfer simulations for L=5mm SS316: (a) Surface plot of e(x,z) (b) Pseudo-color image of e(x,z)

3. COMSOL Modeling of Internal Defect Detection

3.1. Basic Principles of Internal Flaw Detection with Thermal Tomography

Internal material flaws, which are localized regions of lower density compared to the host matrix, can be detected with thermal tomography by observing surface temperature transients. The basic principle that flaw with lower density provides thermal resistance to diffusing heat flux. This causes appearance of temperature gradient on the material surface due to spatial variation of temperature decay. In particular, temperature "hot spots" can be observed on the material surface above the flaw. To visualize flaw detection, COMSOL simulations were performed for a structure consisting a 5cmx5cmx1cm metallic plate with cylindrical flat bottom hole (FBH) defects. An example of a structure used in simulations, consisting of a stainless steel plate with a 5mm diameter, 3mm deep FBH defect is shown in Figure 6. An FBH is a common model of material flaw used in thermal tomography calibration studies. The FBH defect was filled with air to approximately model the un-sintered powder in AM defects which has a lower density and hence lower thermal conductivity than that of the metallic plate

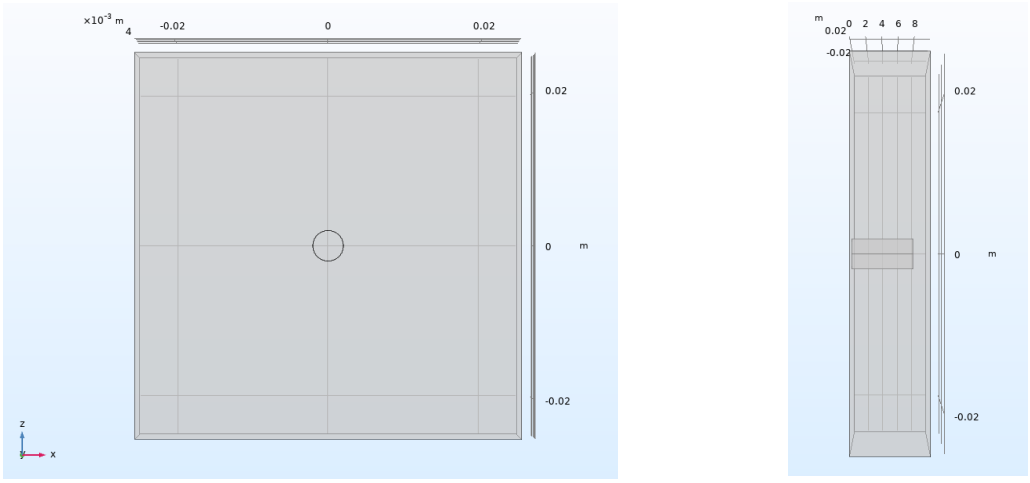

(a) (b)

Figure 6 – View of COMSOL model metallic plate with cylindrical FBH defect in the center: (a) Front (b) Side

Appearance of the "hot spot" can be observed in the sequence of frames shown in Figure 7, which displays time evolution of heat transfer through a metallic plate with an FBH defect. Pseudo-color map with warm colors (red, yellow) corresponding to higher temperatures and cold colors (green, blue) corresponding to lower temperatures is used for display temperature distribution. A uniform thermal pulse of energy incident from the right propagates through the material until encountering an internal defect. Thermal diffusion in the region above the defect is therefore reduced as a result of this metal to air discontinuity which creates a "hot spot," seen on the front surface of the plate. The radius of the FBH is directly related to the radius of the "hot spot." The

latter increases in size over time due to diffusion of heat around the surface of the FBH in the radial direction. A procedure for finding the best threshold criteria to measure the radius of the FBH defect from surface temperature observations is discussed in the next section.

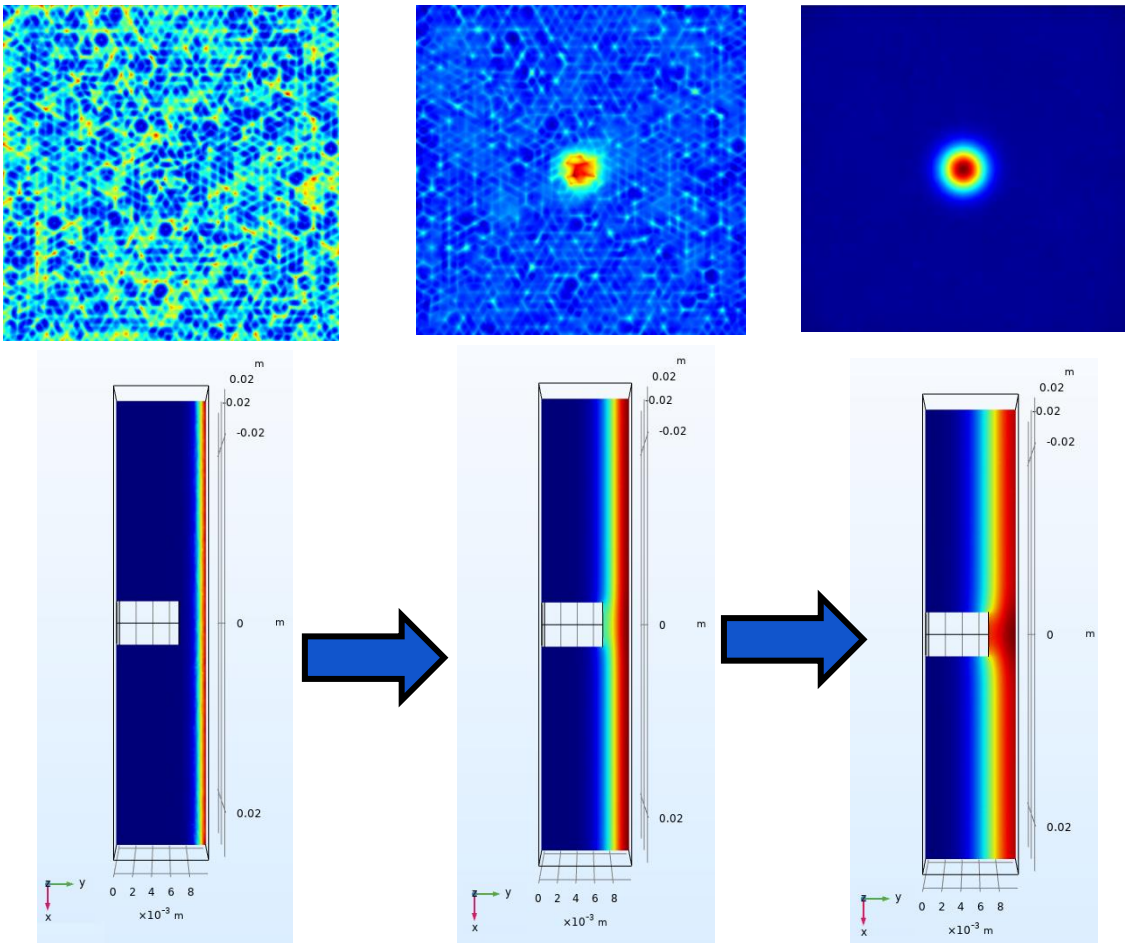

Figure 7 – Time evolution of heat transfer through metallic plate (bottom) and concurrent appearance of localized "hot spot" on the plate front surface (top)

3.2. Estimation of Internal Defect Transverse Size from COMSOL Simulations

A procedure for estimating transverse size of internal defects based on observations of surface temperature transients was developed and evaluated using COMSOL simulations. Estimation of flaw size in simulations was accomplished by collecting 1D temperature data across a center line on the front surface of the plate, as shown in Figure 8. We determined radial temperature distribution of the surface "hot spot" is Gaussian, which is expected since the governing process is diffusion. Therefore, we defined the radius of the "hot spot" to be the distance from the center of the spot where temperature has the maximum value to the point where the temperature decreases by a factor of 1/e. For a Gaussian distribution with standard deviation σ, the radius at 1/e of the maximum temperature would be represented by $\sqrt{2}\sigma$. An example of Gaussian curve fitting is shown below in Figure 8 for the case of a 5mm diameter FBH defect located at 2mm depth below the surface of the plate. Temperature along the line drawn on the surface of the 5cmx5cmx1cm

plate in Figure 8(a) at time t=0.21s after heat pulse application is plotted in Figure 8(b). A Gaussian fit is shown to closely agree with the temperature data.

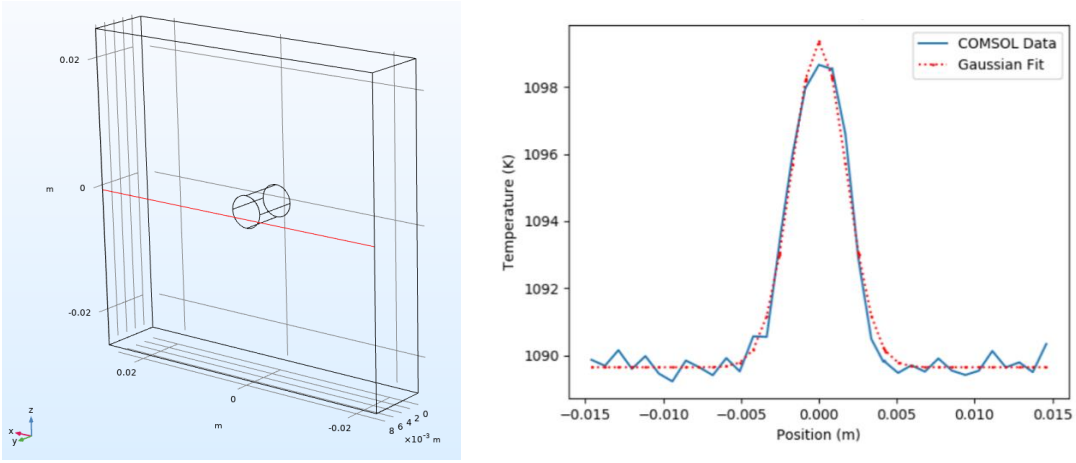

(a) (b)

Figure 8 – (a) Model showing line of surface temperature data collection (b) A Gaussian curve fit to COMSOL data at time t=0.21s

We observed that the "hot spot" radius increases with time, which we attribute to heat diffusion around the FBH cylindrical surface. An example of this phenomena is displayed in Figure 9 for the plate in Figure 8 with 5mm diameter FBH located at 2mm depth. The radius of the "hot spot" almost doubles in 2s. Thus, one has to define a time to measure the "hot spot" to obtain the most accurate estimate of the FBH size. This earliest observation time was chosen based on the sensitivity of the IR camera used in experiment. This study focuses on high-end cameras (e.g. FLIR X8501sc) with noise equivalent temperature difference (NETD) of 20mK to find the limit to defect detection. For more compact but less sensitive cameras (e.g. FLIR A65sc) with NETD of 50mk, the criteria for radial detection will be slightly different.

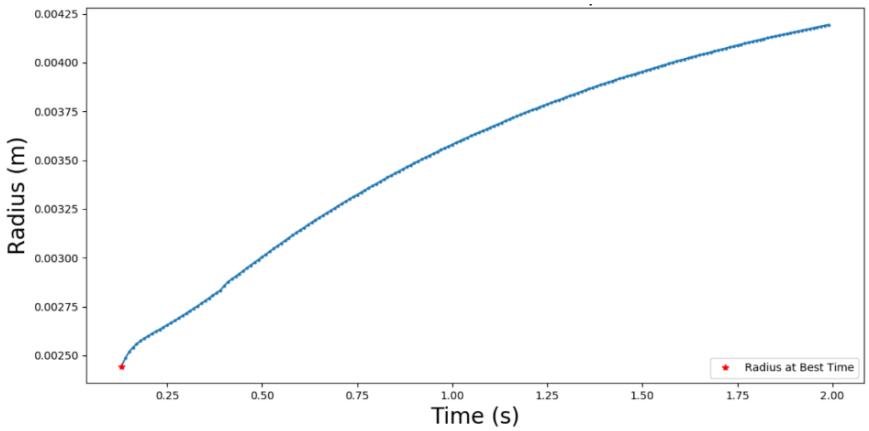

Figure 9 – Increase of observed radius on plate surface with time for a 5mm diameter FBH located at 2mm depth

By selecting the time at which the "hot spot" temperature begins to exceed 20mK relative to the average plate temperature, one could determine the best time for FBH radius estimation. This time

represented the start of "hot spot" appearance on the surface, at which point the radius of the "hot spot" provides the best approximation to the internal defect radius.

To further elucidate the validity of this criteria, Figure 10 shows the divergence of temperature decay curves at a region directly above the defect, and near the edge of the plate (several centimeters away from the defect). The time at which the two curves begin to diverge for the first time corresponds to the time at which the "hot spot" first begins to appear on the plate surface.

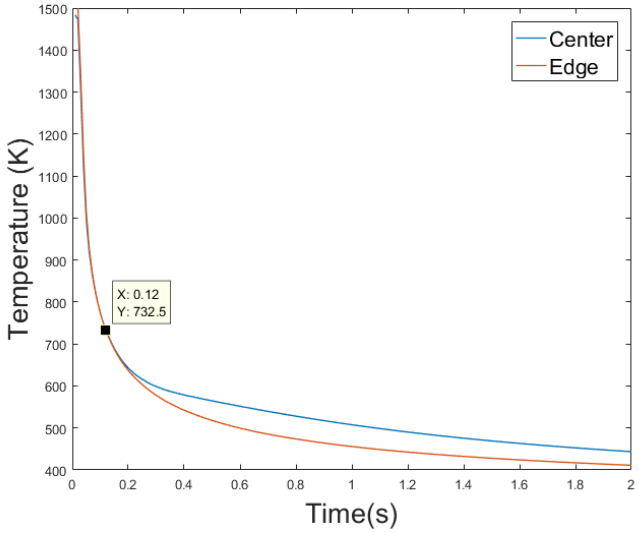

Figure 10 – Estimate of best time for defect detection for 5mm diameter, 2mm deep FBH based on temperature contrast on the plate

It is important to note that radial estimates of internal defects closer to the surface of the metallic plate are more accurate than those for defects located deeper within the plate. Given enough time for the heat to traverse the plate, the "hot spots" eventually appear on the surface of the plate regardless of how deep the defect is. However, accuracy of transverse size and depth location of the flaw estimates progressively decreases due to the effects of thermal diffusion. During the initial period, heat diffusion is predominantly in 1D. However, with increasing time and depth within the plate, heat diffuses in lateral directions as well, which leads to blurring of the "hot spot" and decrease in the accuracy of radius and depth estimation of the FBH. Tables 1 through 4 show variation of "hot spot" observed radii in COMSOL simulations of FBH located at various depths in 5cmx5cmx1cm plates. The smallest temperature difference represents the difference between the peak of a temperature curve directly above the defect and the average temperature near the edge of the plate. This value decreases with increasing FBH depth because heat diffuses through larger volume. Table 1 shows the data for 2.5mm radius FBH in SS316. Table 2 provides data for a smaller 0.5mm radius FBH in the same material SS316. Tables 3 and 4 show results for 2.5mm radius FBH in IN718 and SS304. Values of the observed radius appear to fluctuate slightly with increasing FBH depth, with the general trend indicating increase of the observed radius value and larger deviation of the actual FBH value. Fluctuations of radius size could be attributed to dependence of the onset of lateral heat diffusion on the depth of the FBH.

Table 1 – SS316, 2.5mm radius FBH

Depth (mm)	Time (s)	Smallest Temp. Difference (K)	Observed Radius (mm)
1	0.06	45.00	2.65
2	0.12	2.78	2.45
3	0.25	0.51	3.28
4	0.42	0.22	2.93
5	0.68	0.14	3.26

Table 2 – SS316, 0.5 mm radius FBH

Depth (mm)	Time (s)	Smallest Temp. Difference (K)	Observed Radius (mm)
1	0.06	23.48	0.92
2	0.16	1.06	1.27
3	0.34	0.30	2.24
4	0.63	0.13	2.68

Table 3 – Inconel 718, 2.5mm radius FBH

Depth (mm)	Time (s)	Smallest Temp. Difference (K)	Observed Radius (mm)
1	0.02	8.34	2.74
2	0.05	1.99	2.23
3	0.09	0.41	3.36
4	0.14	0.13	2.90
5	0.21	0.073	2.85
6	0.28	0.025	3.82
7	0.43	0.024	3.95

Table 4 – SS304, 2.5 mm radius FBH

Depth (mm)	Time (s)	Smallest Temp. Difference (K)	Observed Radius (mm)
1	0.05	24.94	3.01
2	0.13	2.56	3.35
3	0.26	0.61	3.14
4	0.42	0.23	3.16
5	0.67	0.12	3.43

3.3. Defect Reconstruction from COMSOL Simulations

As described in Section 2.1, effusivity reconstruction algorithm uses time-dependent surface temperature data to create an image of defect within the metallic plate. Following validation study described in Section 2.2, inversion algorithm was applied to COMSOL simulations data for a SS316 metallic plate with 5cmx5cm cross-section containing an internal FBH defect. Reconstructions performed for 5mm diameter FBH located 1mm depth in 5mm and 10mm thick SS316 plates are shown in Figures 11 and 12, respectively. Reconstruction of effusivity for 5mm diameter FBH located 3mm depth in 10mm thick SS316 plate is shown in Figure 13. All figures shows 3D surface plots and pseudo-color images of e(x,z). In all figures, thermal pulse is incident from the left. Warmer red colors signify the heat propagation through the plate and colder blue tones show the front and end boundaries of the metallic plate.

The images of reconstructed effusivity show that the depth of the defect is correctly determined from the inversion algorithm. The first minima in the effusivity plots represent the approximate location of the top of the FBH defect. Effusivity drops to near zero once the heat propagates to the surface of the high thermal resistance barrier. The effusivity then increases due to the effects of heat diffusion occurring around the cylindrical surface of the FBH. After reaching a maximum, the effusivity decreases once again to represent heat propagation at the end of the metallic plate.

There is noticeable spread in the shape of the cylindrical FBH further within the plate caused by increased radial heat diffusion around the defect with higher thermal resistance. Thus, size detection using the inversion algorithm is more difficult at larger depths when the imaging resolution begins to degrade. At the same time, the inversion algorithm provides a good estimate of the depth of the FBH.

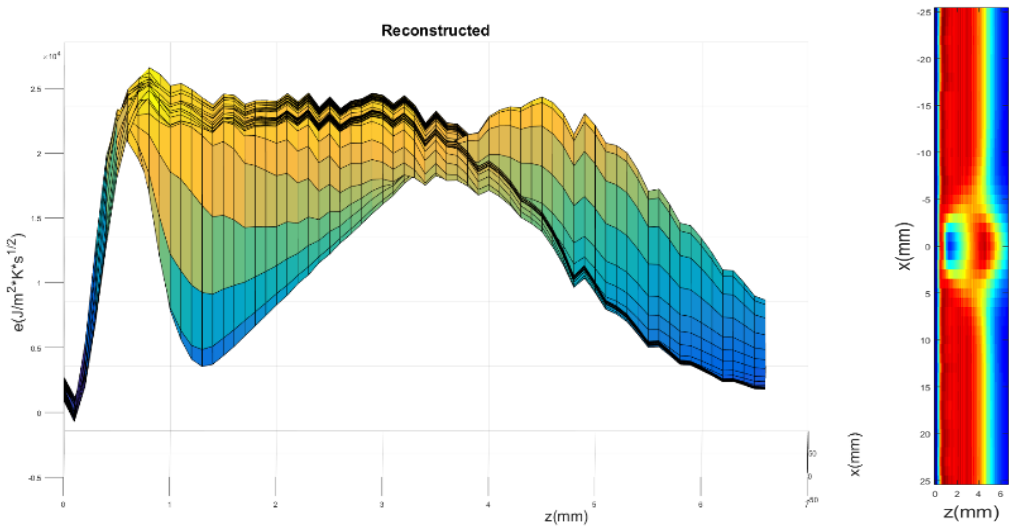

(a) (b)

Figure 11 – Reconstructed effusivity for 5mm diameter FBH located at 1mm depth in 5mm thick SS316 plate (a) Surface plot of e(x,z) (b) Pseudo-color image of e(x,z)

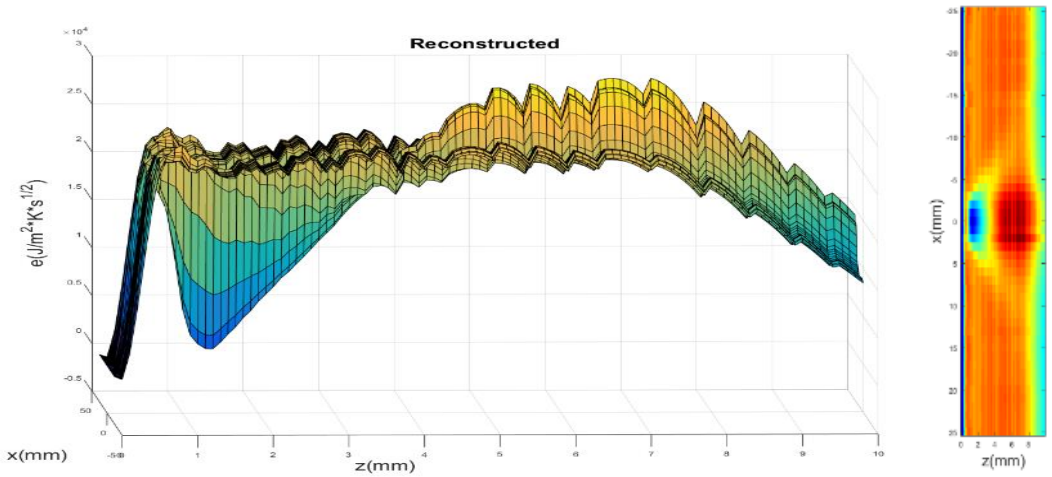

(a) (b)

Figure 12 – Reconstructed effusivity for 5mm diameter FBH located at 1mm depth in 10mm thick SS316 plate (a) Surface plot of e(x,z) (b) Pseudo-color image of e(x,z)

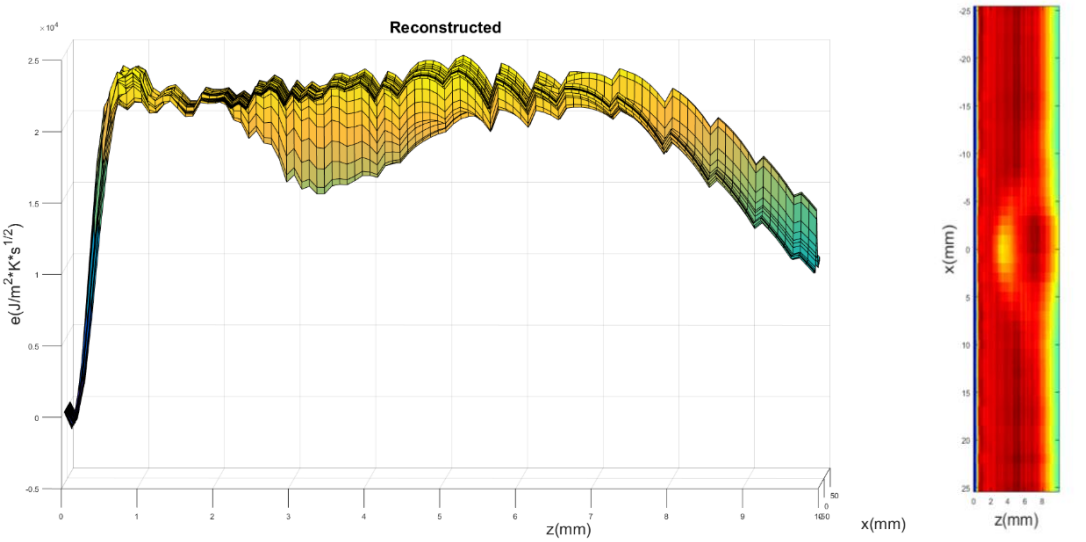

(a) (b)

Figure 13 – Reconstructed effusivity for 5mm diameter FBH defect located at 3mm depth in 10mm thick SS316 plate: (a) Surface plot of e(x,z) (b) Pseudo-color image of e(x,z)

3.4. Estimated Limits of Defect Size Detection from COMSOL Simulations

PTT performance limits on internal defect size detection were analyzed by using both effusivity reconstruction and "hot spot" size estimation methods using the 20mK temperature difference threshold. COMSOL computer simulations were performed for 5cmx5cmx0.5cm SS316 plates with internal cylindrical FBH defects. An example detection and estimation of effective size of a 200µm diameter from the "hot spot" appearing on the surface of the metallic plate is shown in Figure 14. As discussed in Section 3.2, the size of the defect is estimated from the standard deviation σ by fitting a Gaussian curve to the temperature profile.

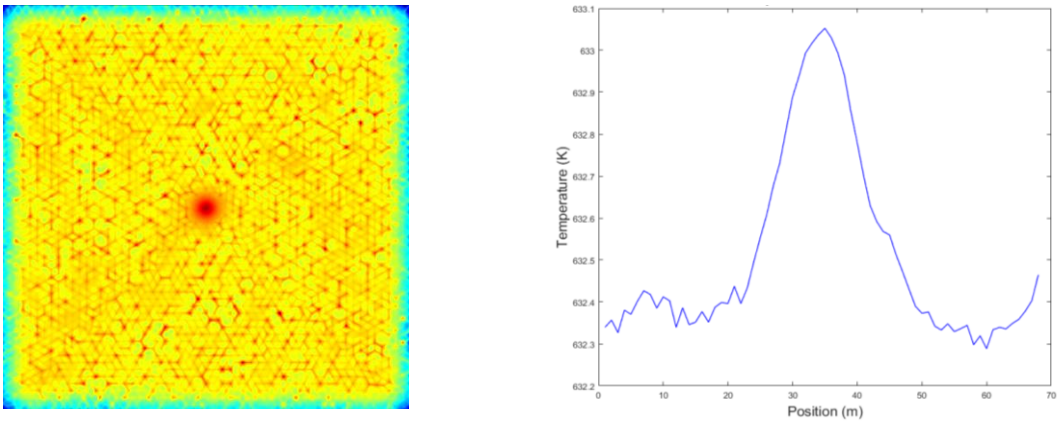

(a) (b)

Figure 14 – (a) "Hot spot" formation for 200µm diameter FBH (b) Surface temperature profile at 0.3s

Table 5 lists the results for smallest detected diameter of an FBH with corresponding maximum depth of the defect. In general, smaller defects are detectable when they are located closer to the surface. The smallest detectable defect is 50µm diameter, which can be detected at the maximum depth of 0.5mm.

Table 5 – Estimated detection limits for cylindrical FBH defects in SS316

Diameter (µm)	Depth (mm)	Smallest Temp. Difference (mK)
50	0.5	40
70	1	23
200	3	20
700	5	33

Reconstructions of effusivity were also performed to evaluate the capability of inversion algorithm in imaging the smallest defects. Based on results of computer simulations, reconstructions at depths greater than 3mm, have relatively low signal to noise ratio (S/N). Reconstructions with higher S/N would require a larger heat flux (e.g. 10x) than what is currently delivered by the flash lamp in the PTT experimental setup shown in Figure 1. Reconstructed effusivity for a 5mm thick SS316 plate containing a 200µm FBH at 1mm depth is shown in Figure 15. The incident heat is amplified by a factor of 10 relative to COMSOL simulations in previous figures to achieve better

imaging contrast. The figure shows 3D surface plot and pseudo-color image of reconstructed e(x,z).

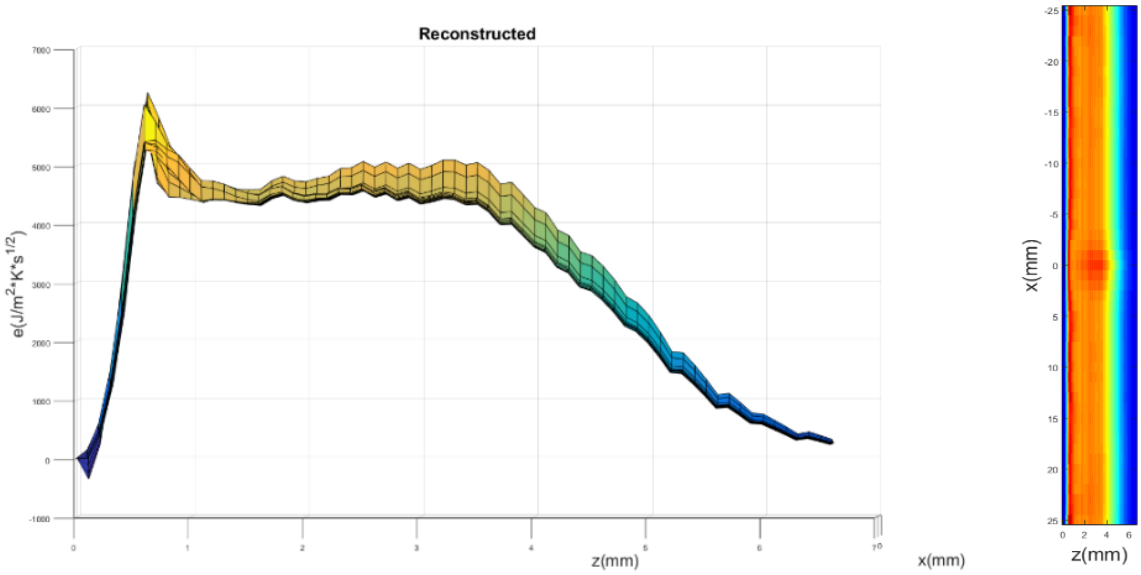

(a) (b)

Figure 15 – Reconstructed effusivity for a 200µm diameter FBH defect located 1mm depth in 5mm thick SS316 plate (a) Surface plot of e(x,z) (b) Pseudo-color image of e(x,z)

While FBH is a common model of material flaw in thermal tomography, more realistic model of a defect observed in powder laser sintering-based AM of metals is that of a sphere. Preliminary COMSOL simulations were conducted to model detection of spherical defects in metallic plates. Reconstructions of effusivity were performed for 5cmx5xmx0.5cm SS316 plate containing hollow spheres with diameters of 3mm, 1mm and 200µm, all located at 1mm depth as measured from the plate surface to the top of respective sphere. Reconstructed effusivity for plates containing 3mm, 1mm and 200µm diameter spheres is shown in Figures 16, 17 and 18, respectively. Each figure displays surface plot and pseudo-color image of e(x,z). To achieve better contrast in reconstructed image, heat flux was increased by factors of 3 and 10. As seen from reconstructed effusivity plot, the depths of the spheres are accurately measured. Future work will examine detection of spherical-shaped defects in greater detail.

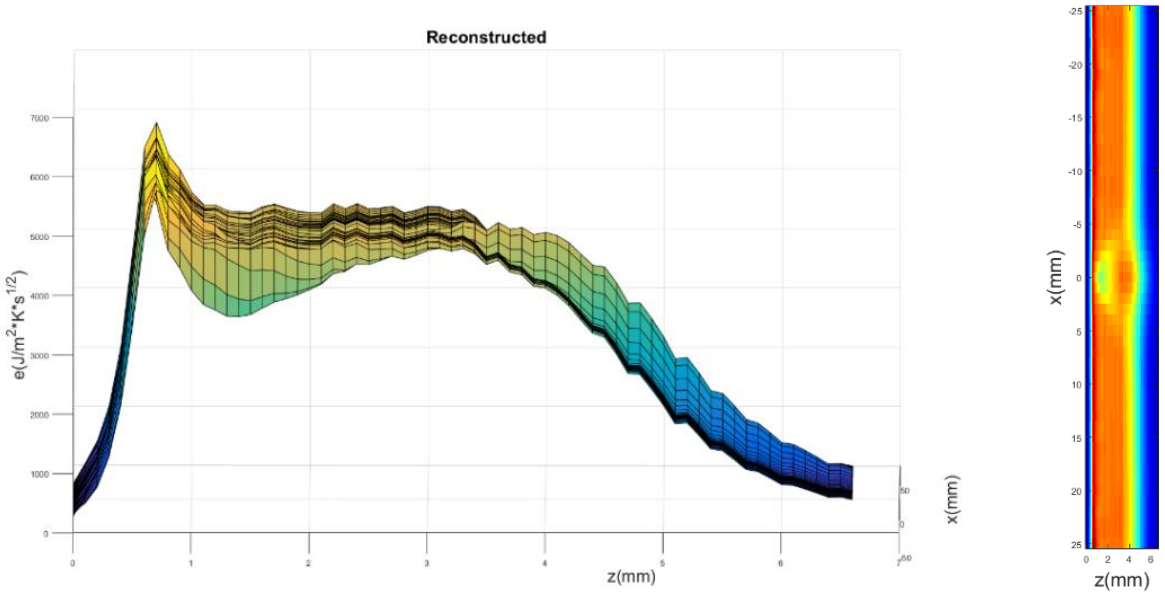

(a) (b)

Figure 16 – Reconstructed effusivity for spherical defect with 3mm diameter (a) Surface plot of e(x,z) (b) Pseudo-color image of e(x,z)

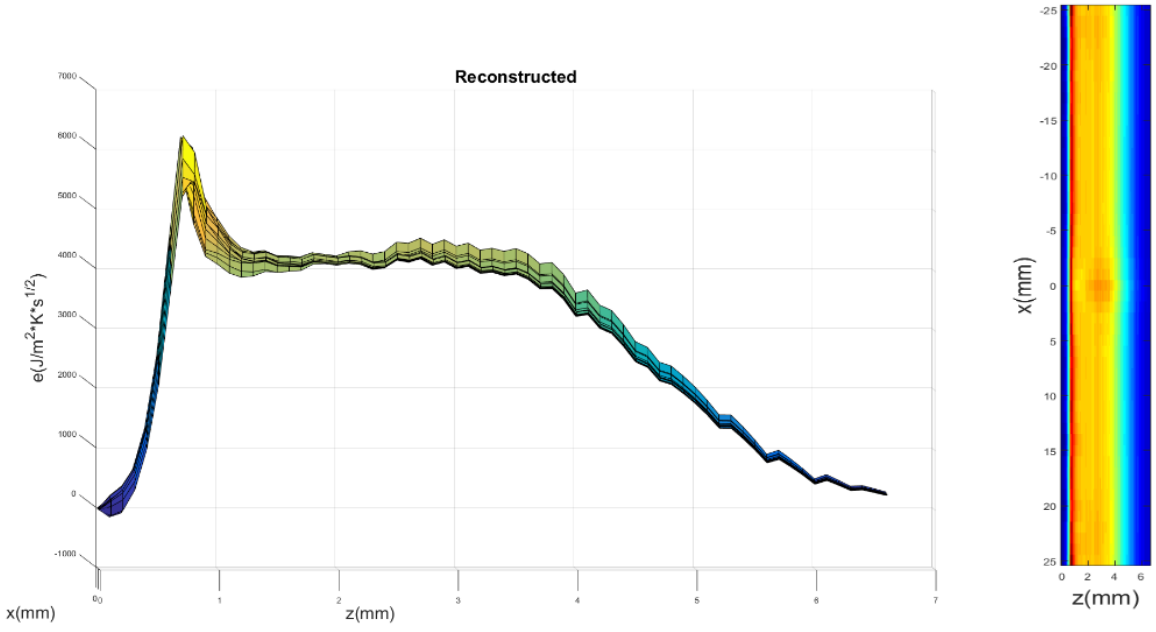

(a) (b)

Figure 17 – Reconstructed effusivity for spherical defect with 1mm diameter (a) Surface plot of e(x,z) (b) Pseudo-color image of e(x,z)

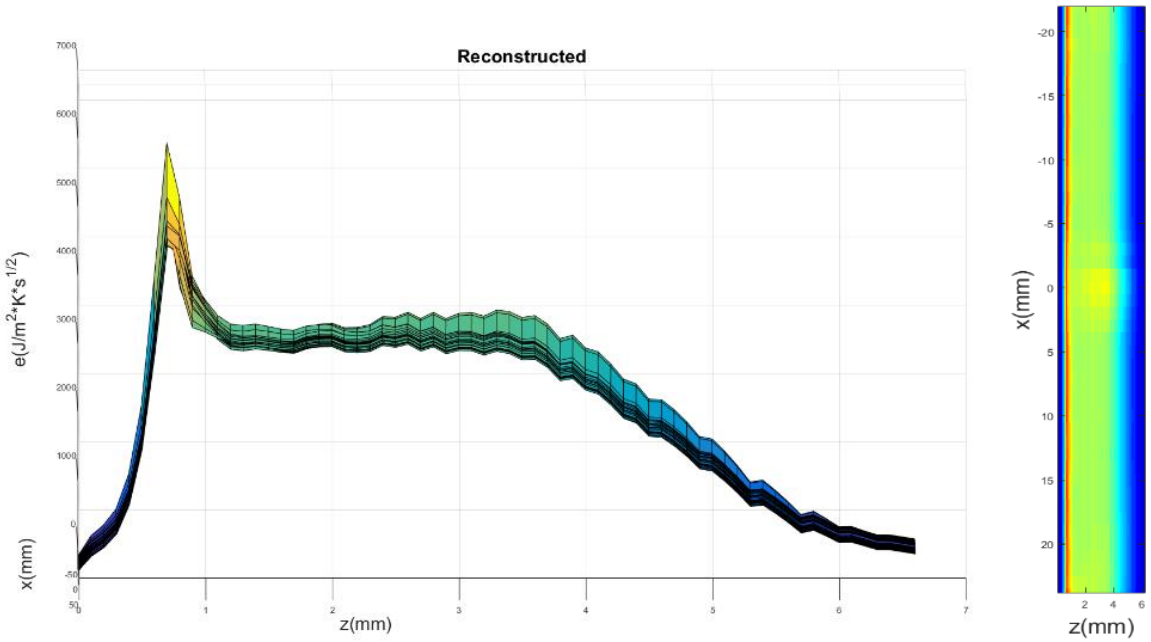

(a) (b)

Figure 18 – Reconstructed effusivity for spherical defect with 200µm diameter (a) Surface plot of e(x,z) (b) Pseudo-color image of e(x,z)

4. Conclusions

This study investigated the limits of pulsed thermal tomography (PTT) capability in detection of defects in metallic plates using COMSOL numerical modeling of heat transfer. Defects are modeled as cylindrical flat bottom holes (FBH), which is a common model of calibrated material flaws in thermal tomography experiments. Materials considered in this study include stainless steel 316 (SS316), stainless steel 304 (SS304), and Inconel 718. Theoretical analyses were conducted to validate inversion of simulated PTT data with COMSOL for a plate. Subsequently, 3D reconstructions were performed on COMSOL simulations for FBH, revealing a decrease in spatial resolution over depth due to thermal diffusion. The results of this study show that the performance of the inversion algorithm for detecting smaller defects depends strongly on the depth of the defect as well as the incident heat flux. The size of detectable defect was estimated by fitting a Gaussian function to surface temperature profile. The criteria for detectability was taken as 20mK noise equivalent temperature difference (NETD), which is currently the sensitivity limit of high-performance infrared cameras. It was determined through COMSOL simulations that the smallest detectable FBH in SS316 has a 50μm diameter and is located 0.5mm below the plate surface.

Next phase of the project work will investigate detection of spherical-shape defects in metallic plates. In addition, experimental validations of algorithms described in this report will be performed with calibrated defects imprinted into the AM specimens.

References

Balageas, D. L., Krapez, J. C., and Cielo, P., (1986). "Pulsed Photothermal Modeling of Layered Materials," J. Appl. Phys., 59(2), pp. 348–357.

Bertali, G., Wang, Y., Lim, J., Scenini, F., Long, C., Freyer, P., and Burke, M. (2015). "Microstructural Analysis of 3D-Printed Alloy 718," Microscopy and Microanalysis, 21(S3), 463-464.

Cunningham, R., Narra, S. P., Montgomery, C., Beuth, J., & Rollett, A. D. (2017). Synchrotron-based X-ray microtomography characterization of the effect of processing variables on porosity formation in laser power-bed additive manufacturing of Ti-6Al-4V. *Jom*, *69*(3), 479-484.

Freyer, P.D., Cleary, W.T., Ruminski, E.M., Long, C.J., Xu, P. (2018). "Hot Cell Tensile Testing of Neutron Irradiated Additively Manufactured Type 316L Stainless Steel," Proceedings of the 18th International Conference on Environmental Degradation of Materials in Nuclear Power Systems -- Water Reactors: Volume 1, 1021-1038.

Heifetz A., Sun J.G., Elmer T., Shribak D., Saboriendo B., Kozak P., Bakhtiari S., Cleary W., Khaykovich B. (2019). "PTT System Performance Evaluation in 3-D Imaging of Calibrated Defects," Argonne National Laboratory, ANL-19/12

Kim C.S. (1975) "Thermophysical properties of stainless steels," Argonne National Laboratory ANL-75-55.

Kempen, K., Yasa, E., Thijs, L., Kruth, J. P., & Van Humbeeck, J. (2011). Microstructure and mechanical properties of Selective Laser Melted 18Ni-300 steel. *Physics Procedia*, *12*, 255-263.

Kultgen D., Grandy C., Kent E., Weathered M., Andujar D., and Reavis A. (2018). "Mechanisms Engineering Test Lopp – Phase I Status Report – FY2018," Argonne National Laboratory ANL-ART-148, ANL-METL-14.

Lewandowski, J. J., & Seifi, M. (2016). Metal additive manufacturing: a review of mechanical properties. *Annual Review of Materials Research*, *46*, 151-186.

Parker, W. J., Jenkins, R. J., Butler, C. P., and Abbott, G. L., (1961). "Flash Method of Determining Thermal Diffusivity, Heat Capacity, and Thermal Conductivity," J. Appl. Phys., 32(9), pp. 1679–1684.

Sames, W. J., List, F. A., Pannala, S., Dehoff, R. R., & Babu, S. S. (2016). The metallurgy and processing science of metal additive manufacturing. *International Materials Reviews*, *61*(5), 315-360.

Sun J.G. (2016). "Quantitative three-dimensional imaging of heterogeneous materials by thermal tomography," Journal of Heat Transfer 138, 112004.

Sun J.G. (2014). "Pulsed thermal imaging measurement of thermal properties for thermal barrier coatings based on a multilayer heat transfer model," Journal of Heat Transfer 136, 081601.

Wakamatsu M., Nei H., and Hashiguchi K., (1995), "Attenuation of temperature fluctuations in thermal striping," *J. Nucl. Sci. Technol.*, vol. 32, no. 8, pp. 752–762.

Zhao, C., Fezzaa, K., Cunningham, R. W., Wen, H., Carlo, F., Chen, L., & Sun, T. (2017). Real-time monitoring of laser powder bed fusion process using high-speed X-ray imaging and diffraction. *Scientific reports*, *7*(1), 3602.

Nuclear Science and Engineering (NSE) Division
Argonne National Laboratory
9700 South Cass Avenue, Bldg. 208
Argonne, IL 60439

www.anl.gov